Photoemission study of twisted monolayers and bilayers of WSe_2 on graphite substrates

Bharti Parashar,[1,2] Lars Rathmann,[3] Hyun-Jung Kim,[4] Iulia Cojocariu,[1] Aaron Bostwick,[5] Chris Jozwiak,[5] Eli Rotenberg,[5] José Avila,[6] Pavel Dudin,[6] Vitaliy Feyer,[1] Christoph Stampfer,[3,7] Bernd Beschoten,[3,8] Gustav Bihlmayer,[4] Claus M. Schneider,[1,2,9] and Lukasz Plucinski[1,*]

[1]*Peter Grünberg Institut (PGI-6), Forschungszentrum Jülich GmbH, 52428 Jülich, Germany*
[2]*Fakultät für Physik, Universität Duisburg-Essen, 47048 Duisburg, Germany*
[3]*2nd Institute of Physics and JARA-FIT, RWTH Aachen University, 52074 Aachen, Germany*
[4]*Peter Grünberg Institute (PGI-1) and Institute for Advanced Simulation (IAS-1), Forschungszentrum Jülich GmbH and JARA, 52425 Jülich, Germany*
[5]*Advanced Light Source, Lawrence Berkeley National Laboratory, One Cyclotron Road, Berkeley, California 94720, USA*
[6]*Synchrotron-SOLEIL, Université Paris-Saclay, Saint-Aubin, BP48, F91192 Gif sur Yvette, France*
[7]*Peter Grünberg Institut (PGI-9), Forschungszentrum Jülich GmbH, 52428 Jülich, Germany*
[8]*JARA-FIT Institute for Quantum Information, Forschungszentrum Jülich GmbH and RWTH Aachen University, 52074 Aachen, Germany*
[9]*Physics Department, University of California, Davis, California 95616, USA*

(Received 18 December 2022; accepted 17 February 2023; published 14 April 2023)

Using microfocused angle-resolved photoemission spectroscopy we investigated microstructures containing regions of single-layer (SL) and bilayer (BL) WSe_2 on graphite substrates at different twist angles between SL WSe_2 and graphite and within the BL WSe_2. Fermi level electrons emitted from the graphite are sharply focused near their K_{gr} points in the Brillouin zone, and, when passing through the WSe_2, get diffracted to form band replicas readily observed in experimental Fermi surface maps from twisted SL WSe_2/graphite. We investigated two twisted BL WSe_2 at twist angles $\sim 28^\circ$ and $\sim 10^\circ$ and found no evidence of hybridization gaps at the interlayer band-crossing points, that could be precursors of the flat bands at smaller twist angles. Similarly, no such gaps were found for SL WSe_2/graphite. Experimental results are complemented by theoretical density functional theory calculations, which suggest that a formation of hybridization gaps in the WSe_2/graphene (which approximates the experimental WSe_2/graphite system) sensitively depends on the WSe_2 band character at the crossing point with the graphene Dirac band.

DOI: 10.1103/PhysRevMaterials.7.044004

I. INTRODUCTION

Van der Waals materials, such as transition metal dichalcogenides (TMDCs), emerged as an intriguing class of layered compounds that exhibit dramatic changes in the electronic properties when the film thickness is reduced down to a single layer [1]. Additionally, assembling these individual layers with different electronic properties facilitates the idea of realizing artificial stacks of solids, the so-called *van der Waals heterostructures* (HSs) [2]. The HS's design enables tailoring the band alignment at various semiconductor interfaces [3,4] into different types of heterojunctions [5–10]. This approach of material design comprises superposition of two crystal lattices with the same or different atomic registries, which leads to the construction of a long-range periodic superlattice. It often gives rise to a periodic moiré pattern that can emerge either from the different lattice constants or from the twist angle. In particular, the twist angle θ between such layers provides an adjustable degree of freedom as compared to the conventional materials. The potential resulting from the moiré pattern influences lattice electrons, leading to novel emerging properties [11].

Following the prediction of Bistritzer and MacDonald [12], and the demonstration of the gate-controlled superconductivity in twisted bilayer graphene (TBG) [13], similar models have been reported for TMDCs [14–16] predicting fascinating electron correlations and topologies in their twisted bilayer structures. In particular, Wang *et al.* [6] reported experimental evidence of low-energy flat bands in twisted bilayer WSe_2, with signatures of collective phases in transport measurements for twist angles θ between 4° and 5.1°. Recently, Kundu *et al.* [17] have examined the formation of flat bands in twisted BL WSe_2 for twist angles down to 2.28°.

Angle-resolved photoemission (ARPES) is the method of choice for electronic band structure mapping. However, applying this technique to microflakes is challenging, due to their small size, and has become possible only within the last decade following the development of microfocused ARPES (microARPES) techniques [18]. Recent microARPES works on TMDC microflakes have reported band replicas due to scattering on the moiré reciprocal vectors [19], on the moiré potential [20], and θ-dependent hybridization and superlattice effects [21]. Furthermore, recently microARPES provided evidence for flat bands in the magic-angle twisted bilayer graphene [22,23].

In this work, we investigate two types of sample structures: twisted single-layer (SL) WSe_2/graphite and twisted bilayer

*l.plucinski@fz-juelich.de

 ©2023 American Physical Society

(BL) WSe_2/graphite fabricated by mechanical exfoliation technique. These structures exhibit two types of twist angles: between the graphite and WSe_2 and between the top and bottom layers of WSe_2. In BL structures, previously reported double bands at Γ points near the valence band maximum (VBM) [3,24] manifest the interlayer hybridization. They are also confirmed in our theoretical calculations of twisted BL WSe_2, where the splitting of the double bands decreases for the twisted layers, as compared to the aligned BL. Aside from these signatures, in the region of interest near the VBM, the spectra appear as an incoherent sum from the two layers. At our experimental resolution we observe no signs of hybridization gaps that could be precursors of flat bands for smaller twist angles.

In the twisted SL WSe_2/graphite structures, the electrons emitted from the graphite π bands scatter in the SL WSe_2 layer leading to the emergence of multiple copies [19,25] which reflect the trigonal symmetry of a SL WSe_2. We argue that this effect is related neither to the hybridization between SL WSe_2 and graphite, nor to the formation of the moiré lattice, and would be present also for noninteracting layers.

We also performed calculations of the SL WSe_2/graphene that approximate the experimental WSe_2/graphite system. We found that for the topmost valence bands the magnitude of the hybridization gaps between the graphene and WSe_2 in the vicinity of the K point depends on twist angle. This effect is likely related to the out-of-plane orbital contribution to the WSe_2 band character at the band-crossing points, and to the relative alignment of the W $d_{x^2-y^2}$ and graphene p_z orbitals with respect to the position in the Brillouin zone.

II. METHODS

A. Sample preparation

Samples were prepared by using the dry transfer technique, as reported in [26]. Highly oriented pyrolytic graphite (HOPG) was exfoliated on n-doped Si substrate by scotch tape method to obtain flakes with thicknesses ranging from 10 to 40 nm. The graphite flakes serve the purpose of the atomically flat conductive substrate for the flake sample structures. Before the transfer, n-doped Si substrates were ultrasonically cleaned in isopropanol, acetone, and ionized water solvents to remove the native oxide, at an interval of 15 min in each solvent, and then dried with a nitrogen gun. The bulk layered WSe_2 crystal was exfoliated with a scotch tape to obtain atomically thin flakes. These two-dimensional (2D) WSe_2 flakes were transferred onto the polydimethylsiloxane (PDMS) stamp, which was adhered to the glass slide to ease its handling for further processing. The transparent stamp allows us to identify single-layer WSe_2 flakes through the contrast observed using the transmission mode under an optical microscope.

Once we identified a single layer of WSe_2 on the PDMS stamp positioned on the surface of the glass slide, we attached it on the three-axis manipulator facing upside down. Next, the exfoliated thick graphite flake on n-doped Si substrate has been mounted on the XYZ stage using vacuum and the substrate was heated up to 75 °C–100 °C, facilitating the transfer process. By carefully aligning the transparent PDMS stamp, the WSe_2 flakes were then transferred at a submicrometer resolution over a desired location on the thick graphite flake. We repeated the same process for transferring the second monolayer of WSe_2 on top of WSe_2/graphite/n-Si. This way we obtained both SL and BL structures of WSe_2 on graphite/n-Si since both SL and BL parts are present in each microstructure. With this process, we prepared three microstructures (samples A, B, and C) with different twist angles between their constituent layers.

B. Spatially resolved angle-resolved photoemission spectroscopy

Samples A and B were transported to the Microscopic and Electronic Structure Observatory (MAESTRO) at the Advanced Light Source. The samples were annealed at 300 °C for several hours prior to the measurement in order to desorb adsorbates. The microARPES measurements were performed at the *nanoARPES* end station at a base pressure lower than 5×10^{-11} mbar at primarily a photon energy of 147 eV and using a focusing capillary that produced a beam spot size of approximately 1 μm [27]. The data were collected using a modified Scienta R4000 hemispherical electron analyzer. All measurements were carried out at 40 K.

Additional microARPES measurements were conducted at the ANTARES beamline of the Soleil synchrotron facility on sample A. Before the measurements, we followed the same sample preparation procedures as those used at MAESTRO beam line. At ANTARES, by the utilization of Fresnel zone plate optics, the beam was focused to ∼0.6 μm. All of the measurements were carried out at $h\nu = 100$ eV with p-polarized light and at 100 K.

Further experiments on atomically thin SL WSe_2/graphite microstructure (sample C) were performed at the NanoESCA beam line of Elettra, Trieste, with beam spot size of 10–15 μm using a modified FOCUS NanoESCA momentum microscope. Before the experiments, the sample was subjected to the same preparation processes as at the other beam lines. A homogeneous region on the sample surface was identified by using the photoemission electron microscopy (PEEM) in real space with high-pressure Hg lamp as an excitation source. Moreover, unlike traditional ARPES setups, momentum microscope scans the complete half-space emission without rotating the sample and enables high linearity in the $k_{||x}$ vs $k_{||y}$ maps. All measurements at the NanoESCA were taken at 80 K using $h\nu = 40$ eV p-polarized light.

C. Density functional theory calculations

To investigate the twisted SL WSe_2/graphene and twisted BL WSe_2, we performed density functional theory (DFT) calculations using the VASP code [28,29]. Projector augmented wave potentials [30] were employed to describe the valence electrons, the electronic wave functions were expanded by a plane-wave basis set with the cutoff energy of 450 eV, and the atomic relaxation was continued until the Hellmann-Feynman force acting on every atom became lower than 0.01 eV/Å. For the exchange correlation functional we use the rev-vdW-DF2 method [31] which includes van der Waals (vdW) interactions and is known to be suitable for the layered transition metal dichalcogenides in predicting lattice parameters and atomic

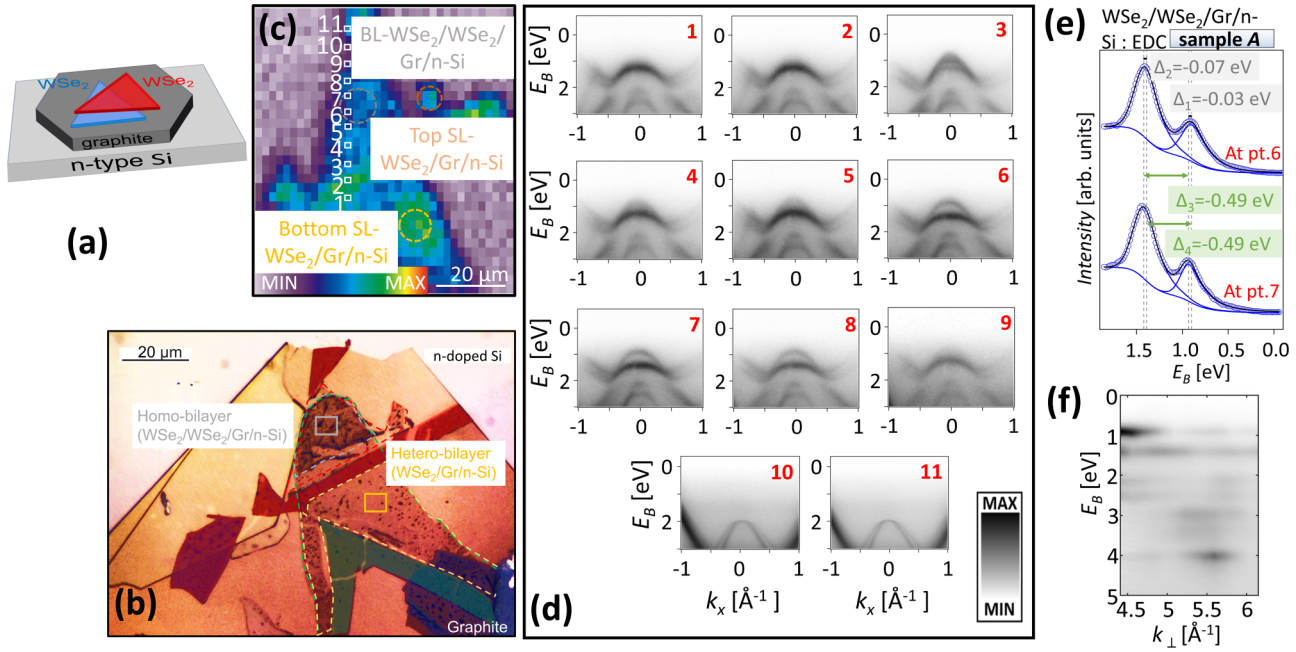

FIG. 1. Characterization of sample *A*. (a) Schematic model of the sample configuration. (b) Optical image and (c) spatial photoemission intensity map. (d) Set of normal emission ARPES maps at $h\nu = 147$ eV at boxes indicated in (c). (e) Normal emission EDCs at boxes 6 and 7. (f) $E_B(k_\perp)$ map at box 7 made from set of normal emission EDCs for $h\nu$ between 80 and 150 eV.

positions [32,33]. The Brillouin zone was sampled using the $11 \times 11 \times 1$ k-point grid for the primitive unit cell of 2H-WSe_2. Band unfolding was performed using the method of Popescu and Zunger [34] as implemented in the VASPBAUM code [35].

Spin-orbit coupling (SOC) was taken into account in the calculation of the electronic structure, but ignored in the structural relaxations, where the impact was found to be negligible.

III. RESULTS

A. Identification of SL and BL microregions

Figure 1(a) shows a schematic arrangement and Fig. 1(b) an optical micrograph of the sample *A* with the SL WSe_2 and twisted BL WSe_2 flakes on graphite at different twist angles. A graphite flake (exfoliated directly on a highly n-doped silicon wafer) serves as an atomically flat conducting substrate. The sample region where any portion of the top WSe_2 monolayer flake covers the bottom monolayer flake of WSe_2 is the BL region. The areas of the overlapping regions of twisted BL WSe_2/graphite and twisted SL WSe_2/graphite flakes are denoted by the gray and yellow dotted lines in Fig. 1(b). Figure 1(c) has been measured by scanning the microfocused beam of photons over the sample surface at a photon energy of 147 eV and measuring photoelectrons emitted from the valence bands at the momenta related to WSe_2. It identifies the same region as shown in the optical image in Fig. 1(b). A similar micrograph from the sample *B* is presented in the Supplemental Material, Fig. S1 [36].

Figure 1(d) depicts a set of ARPES maps at 11 boxes indicated in Fig. 1(c), demonstrating that the microfocused beam spot can precisely select the desired area on the sample, clearly distinguishing between SL [boxes 1 and 2 in Fig. 1(c), single band at the VBM at Γ_0], BL (boxes 6–8, double band at Γ_0), and graphite (boxes 10–11) regions. The double band near the VBM at Γ_0 results from the bonding-antibonding interaction between d_{z^2} and p_z orbitals from the adjacent layers, and is a signature of a BL. Respectively, a single band is a signature of a SL. In Fig. 1(e) we show Voigt fits of the normal emission energy distribution curves (EDCs) from boxes 6 and 7 and identify binding energy shifts of the order of 30 meV. This suggests inhomogeneities and local doping varying on the μm scale on the flake surface within the BL region. The average splitting between bonding and antibonding states at Γ is between 0.48 and 0.52 eV at different positions of samples *A* and *B*. These values are significantly smaller than ∼0.6 eV in nontwisted BL WSe_2 [3,24,37,38], which suggests reduced hybridization in our twisted layers.

Figure 1(f) shows the $E_B(k_\perp)$ map at the BL region made from normal emission EDCs for $h\nu$ between 80 and 150 eV, with the perpendicular momentum $k_\perp = \sqrt{(E_{\rm kin} + V_0)2m/\hbar^2}$, and V_0 set to 10 eV. The bonding-antibonding features near the local VBM at Γ_0 (E_B near 1 and 1.5 eV) are present at all probed $k_\perp$. Furthermore, these states exhibit the expected intensity modulation due to the final-state interference (the matrix element effect), with no other states appearing in this range, indicating that we are exclusively probing the BL region. Qualitatively, the mechanism of this modulation can be explained through a free-electron final state ARPES model [39], where the normal emission free-electron final-state (FEFS) matrix element $\langle e^{ik_{f\perp}\cdot z}|\Psi\rangle$ for the two hybridized layers separated by the distance d is modulated by the factor $1 + e^{ik_\perp \cdot d}$. This will be additionally modulated when taking into account the radial part of the orbital wave function and selections rules [39], while an accurate description of the

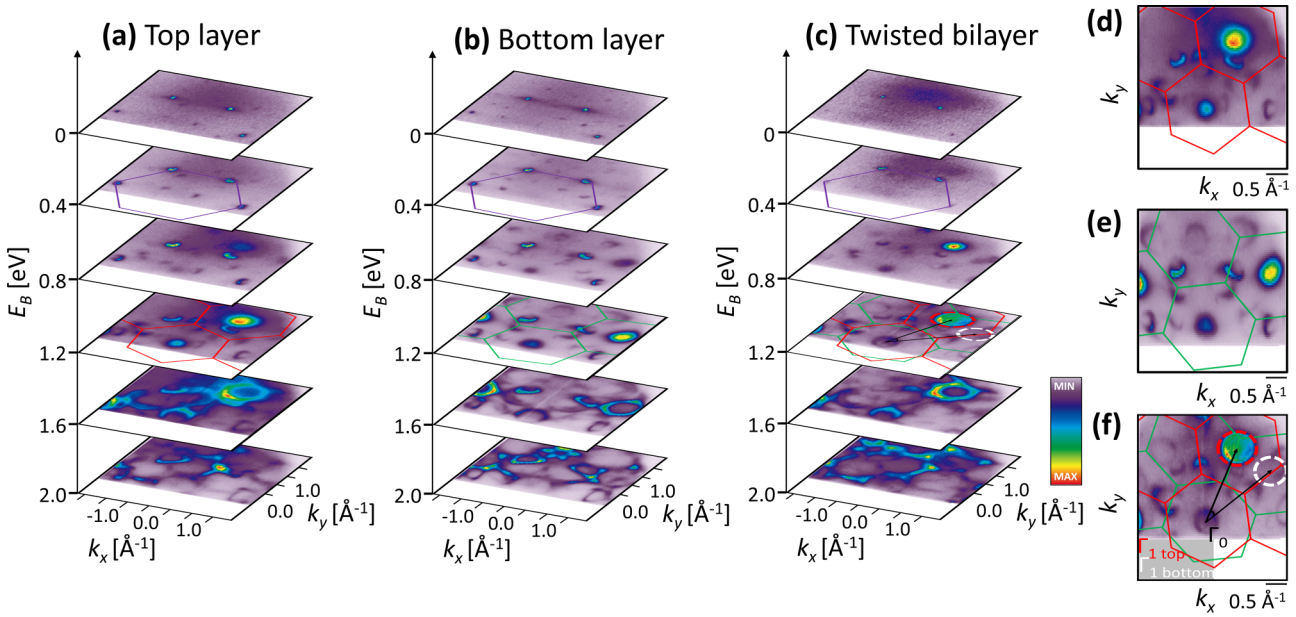

FIG. 2. ARPES spectra from WSe_2 SLs and BL of sample *B*. (a), (b) Show maps from top and bottom SLs, and (c) from the BL. (d)–(f) Show details of the maps for top SL, bottom SL, and BL, respectively, at $E_B = 1.2$ eV. Red and white dashed circles in (f) represent the positions of the Γ_1 from top and bottom layers, and black arrows depict the twist angle.

photoemission process is more complex and uses the time-reversed LEED final state [40].

B. 3D ARPES data sets

Figure 2 shows an overview of $I(E_B, k_x, k_y)$ data sets from sample *B*. The extended measured angular range allows imaging both Γ_0 (center of the first surface BZ, $k_x = k_y = 0$) and Γ_1 (second BZ) points of WSe_2 in a single map. The lower binding energy region shows K_{gr} points of the graphite substrate, depicted by hexagons in maps at $E_B = 0.4$ eV in Figs. 2(a)–2(c). The binding energy region at $E_B = 0.8$ eV and higher contains a mixture of graphite and WSe_2 bands, and in maps at $E_B = 0.8$ eV we identify first and second BZs of the WSe_2 layers through their respective Γ points.

Similar maps for sample *A* are shown in Fig. 3. The details of the Γ_1 region for the BL WSe_2 of sample *A* are shown in Fig. 4. A faint intensity related to the Γ_1 hole pocket of the bottom WSe_2 layer can be identified in Fig. 3(c), and is depicted by the white circle in Fig. 3(d). The intensity ratio between top and bottom layer Γ_1 features is $\sim 5/1$, suggesting an inelastic mean-free path of <1 nm for WSe_2 valence electrons at our photon energy of 147 eV. Figures 4(c)–4(e) show the $E_B(k_x)$ cuts through the Γ_1 points of the top and bottom WSe_2 layers. In Fig. 4(d) the faint shadow related to the hole pocket of the bottom WSe_2 layer can be identified, and it is depicted by the white dotted line in Fig. 4(e). Neither of these maps show the indications of the flat band formations due to the moiré potential of the twisted BL.

Figures 2(d)–2(f) show details of the maps at $E_B = 1.2$ eV. Due to the lack of inversion symmetry, this results in a trigonal symmetry of the WSe_2 monolayer; the intensity of Γ_1 points at neighboring BZs is strongly modulated, with the signal from every second Γ_1 nearly vanishing. This effect is similar to trigonal low-energy electron diffraction (LEED) patterns measured on single-terrace terminations from TMDCs [41]. Interestingly, since the effect is observed in a SL, it indicates that it derives from the direction of the topmost W-Se bonds through the surface sensitivity of ARPES. Since the topmost valence bands at Γ derive almost exclusively from the d_{z^2} orbitals localized on W sites and p_z orbitals localized on Se, the effect can be explained by interference within the FEFS matrix element $\langle e^{i\mathbf{k}_f \cdot \mathbf{r}} | \Psi \rangle$, with positions $\mathbf{r}$ of W and Se sites reflecting the lack of the inversion symmetry, and leading to different phase shifts in the matrix element [42]. However, for a quantitative description one would need to consider a more complete final state.

We can utilize the clear trigonal symmetry of the constant energy maps (CEMs) to unambiguously assign the twist angle as visualized in Figs. 2(f) and 3(d) for samples *B* and *A*, respectively. The detailed analysis is presented in the Supplemental Material, Sec. SV [36], and yielded $\sim 28^\circ$ for sample *B* and $\sim 10^\circ$ for sample *A*. We estimate the accuracy of the twist angle estimation angle from hemispherical analyzer CEMs to be $\pm 1^\circ$ with the uncertainly dominated by intrinsic nonlinearities in the angular scale, in particular with the wide-angle mode ($\sim 36^\circ$) used in this work. These issues originate mostly in the analyzer lens system, and are difficult to correct systematically. We will further discuss them in the later part of the paper.

C. Orbital character and VBM estimation

Figure 5 shows the calculated band structures of a freestanding SL, and aligned AA′ (derived from bulk 2H polytype) and AA (with layers on top of each other) stackings [17,43] for a BL WSe_2. The topmost valence bands are a mixture of out-of-plane d_{z^2} and p_z orbital characters at Γ and

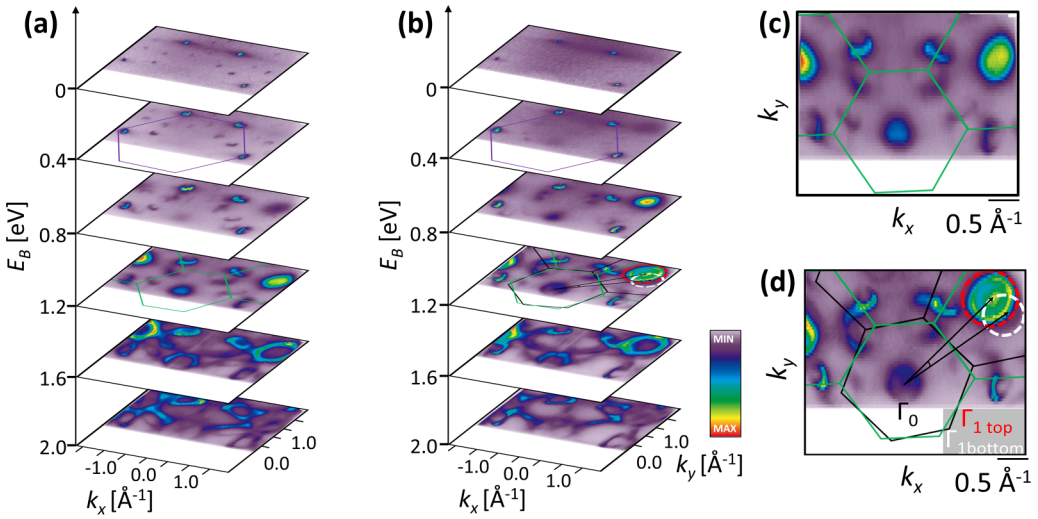

FIG. 3. ARPES spectra from WSe_2 SLs and BL of sample *A*. (a) Shows the maps from the bottom SL and (b) from the BL. (c), (d) Show details of the maps from bottom SL and BL, respectively, at $E_B = 1.2$ eV. Red and white dashed circles in (d) represent the positions of the Γ_1 from top and bottom layers, and black arrows depict the twist angle.

a mixture of in-plane $d_{x^2-y^2}$ and d_{xy} orbital characters at K_W. Figure 6 shows selected maps from the twisted BL of sample *B* measured with *p*- [top row, panels (a)–(c)] and *s*-polarized light [bottom row, panels (d)–(f)]. As expected, the bands near Γ_0 are more intense for *p*-polarized light, due to their out-of-plane orbital character [Fig. 6(b)]. Conversely, bands at K_W are more pronounced for *s*-polarized excitation [Fig. 6(f)]. The VBM of a 2H-stacked BL is at K_W [3], therefore, in the twisted BL, where the interaction between the layers is weaker, the VBM is also expected at K_W. This is indeed the case, as seen from comparing Figs. 6(b) and 6(f). The splitting between the bands at the K_W point is ∼0.48 eV in agreement

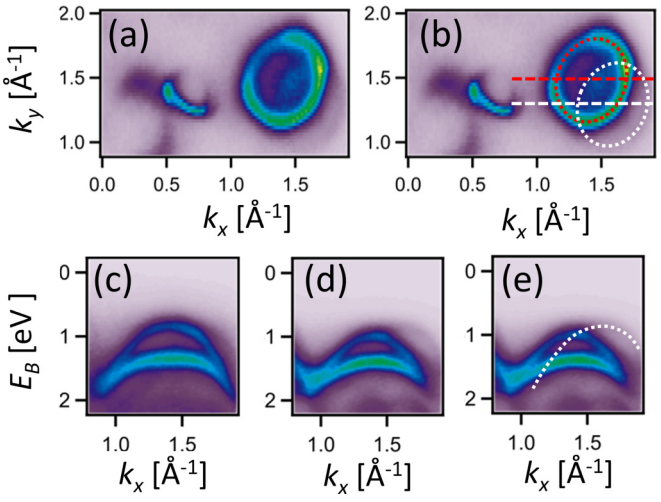

FIG. 4. (a) Details of the spectra from sample *A* near the Γ_1 at $E_B = 1.14$ eV. (b) Same map as in (a) but with red and white circles indicating the positions of Γ_1 from top and bottom layers, respectively. (c), (d) $E_B(k)$ cuts along the red and white dashed lines indicated in (b), respectively. (e) Same as (d) but with the guide line indicating the dispersion of the bottom layer Γ_1 band.

with the previous studies [3,24,44], where values between 0.47 and 0.5 eV were obtained.

Figure 7(a) shows the same map as Fig. 2(d), where the graphite Dirac cone bands are located in the vicinity of the Γ_1 of SL WSe_2. We have focused on this region since the graphite Dirac bands are made from C $2p_z$ and topmost WSe_2 Γ bands from W $5d_{z^2}$ and Se $4p_z$ orbitals that could potentially hybridize, leading to avoided crossings. Previously, such avoided crossings were proposed in monolayer graphene on MoS_2 [45] and in SL MoS_2/graphene [25] through the analysis of the second derivative microARPES spectra. Within our experimental resolution, we observe no sign of such hybridization since the dispersion of the WSe_2 Γ_1 band is unaffected in the region where it crosses with the graphite Dirac band. We took advantage of the "dark corridor" of the Dirac bands [46], where the spectral intensity of one of the Dirac band branches is essentially turned off. This avoids having an incoherent intensity sum the two bands, allowing to inspect any modification of the Γ_1 band separately.

D. Copies of graphite *K*-point Dirac cones

The Fermi surface maps in Figs. 2 and 3 show a set of dotlike features which stem from the graphite Dirac conelike dispersions. These maps are shown in detail in Fig. 8, where one can see a set of intense dots related to graphite K_{gr} point and additional weaker dots which we attribute to their copies. When the electrons emitted from graphite are passing through the WSe_2 monolayer, they can be diffracted leading to first- and higher-order copies in the CEMs. These copies shall appear for all graphite bands, but they are most pronounced near the Fermi level, where K_{gr} points are sharp and no other bands are present. Copies are further characterized to demonstrate their conical dispersion through the CEM at $E_B = 1$ eV [Fig. 8(e)] and comparison between the $E(k)$ map at the zero-order graphite K_{gr} point [Fig. 8(f)] and one of the first-order copies [Fig. 8(g)]. Another case of such diffraction copies has been discussed by Ulstrup *et al.* [19] for a similar

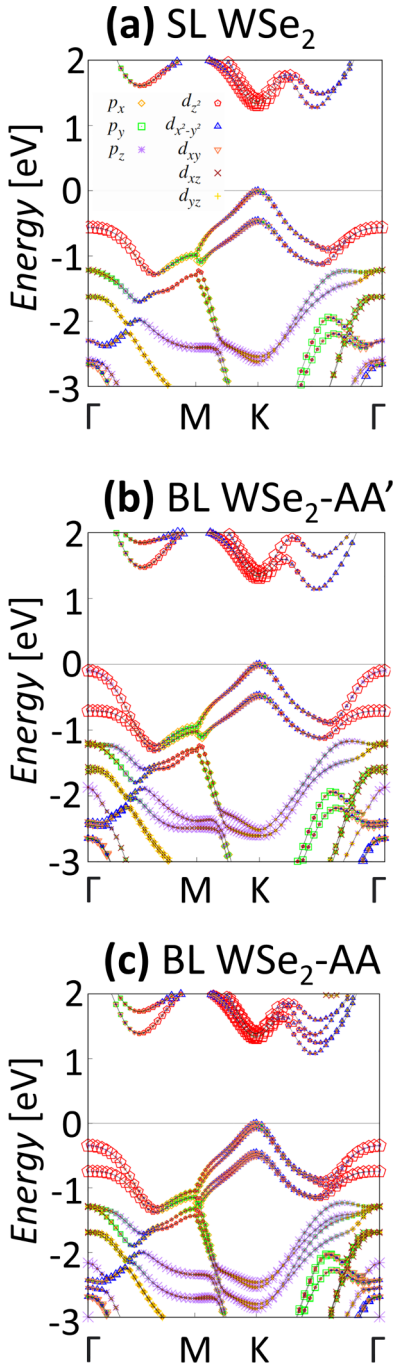

FIG. 5. Calculated orbital characters for the (a) freestanding SL, (b) AA′ (2H) BL, and (c) AA BL WSe_2 [17]. The symbols associated with various orbital characters for Se (p) and W (d) are explained in (a).

interface of graphene/WS_2. Compared to our WSe_2/graphite interface, in their case the sequence of layers is reversed, hence, electrons emitted from WS_2 Γ_0 have been diffracted through the graphene layer.

Mathematically, the wave vectors of the copies can be computed through the reciprocal space vectors of participating layers $\mathbf{G}_W$ and $\mathbf{G}_G$ for WSe_2 and graphite, respectively. We define the twist angle between graphite and WSe_2 as $\theta = \arccos(\frac{\mathbf{G}_W \cdot \mathbf{G}_G}{|\mathbf{G}_W|\,|\mathbf{G}_G|})$ and the moiré vector $\mathbf{G}_m = \mathbf{G}_W - \mathbf{G}_G$.

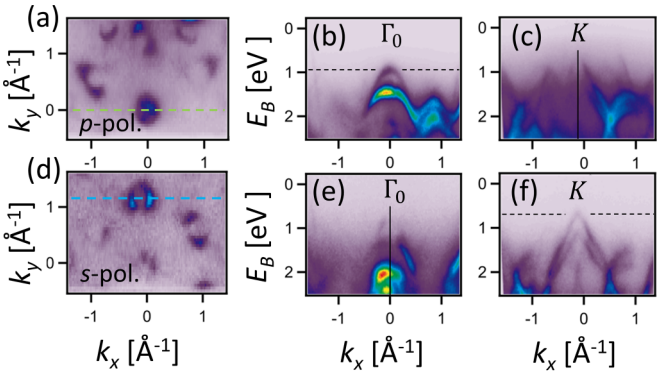

FIG. 6. Selected maps from the BL of sample B. Top row (a)–(c) CEM at $E_B = 1$ eV for p-polarized light. Bottom row (d)–(f) CEM at $E_B = 1$ eV for s-polarized light. Green dashed line in (a) shows the momentum trajectory for maps (b) and (e). Blue dashed line (d) shows the momentum trajectory for (c) and (f). Black dashed lines in (b) and (f) indicate the local VBM at Γ_0 and K points, respectively.

Following Ref. [19] we obtain the angle of the copies as $\phi_m = \arctan(\frac{\sin\theta}{\cos\theta - |\mathbf{G}_G|/|\mathbf{G}_W|})$ and the length of their vectors $|\mathbf{G}_m| = \frac{G_G^2 - |\mathbf{G}_G|\,|\mathbf{G}_W|\cos\theta}{|\mathbf{G}_G|\cos\phi_m}$.

Figures 8(a)–8(d) show the CEMs near the Fermi level ($E_B = 30$ meV) for the *bottom* and *top* SL WSe_2 structures of sample B (*bottom* and *top* refer to the monolayers forming the BL WSe_2 [see Figs. 2(a) and 2(b)]. Figures 8(b) and 8(d) show the same data as 8(a) and 8(c), respectively, but with added simulated positions of the Dirac point copies according to the above equations. The first-order diffraction creates six copies around each K_{gr} point of graphite, at a reciprocal distances of $\mathbf{G}_W$. Some of these $\mathbf{G}_W$ vectors are plotted in Fig. 8(h) to clarify the arrangement of copies near the zone center in Fig. 8(d). Interestingly, in Fig. 8(d) only three out of these six copies can be identified, which we attribute to the lack of inversion symmetry in WSe_2 and the directional bonds, as discussed earlier. We have used $\theta_{WG} = 7^\circ$ for the *bottom* SL [Fig. 8(b)] and $\theta_{WG} = 24^\circ$ for the *top* SL [Fig. 8(d)] to obtain the best overall match with the experiment. We note that the sum of these angles adds to 31°, which does not agree with $\theta = 28^\circ$ determined from Figs. 2(d)–2(f). This is related to the problems in determination of twist angle from the CEMs measured by the hemispherical analyzer, as discussed below.

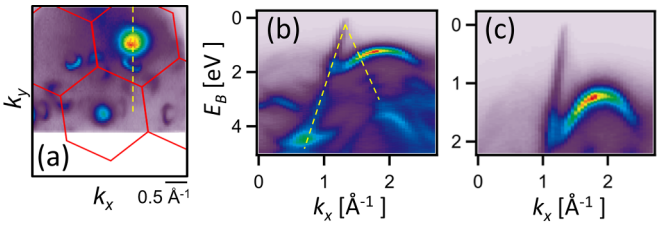

FIG. 7. Crossing between Γ_1 and graphite bands in sample B. (a) CEM at $E_B = 1.2$ eV; yellow dashed line shows the BZ trajectory for maps (b) and (c). (b) $E(k_y)$ showing the region where graphite and Γ_1 band cross; yellow dashed line depicts the graphite Dirac cone dispersion. (c) Magnified region of the crossing.

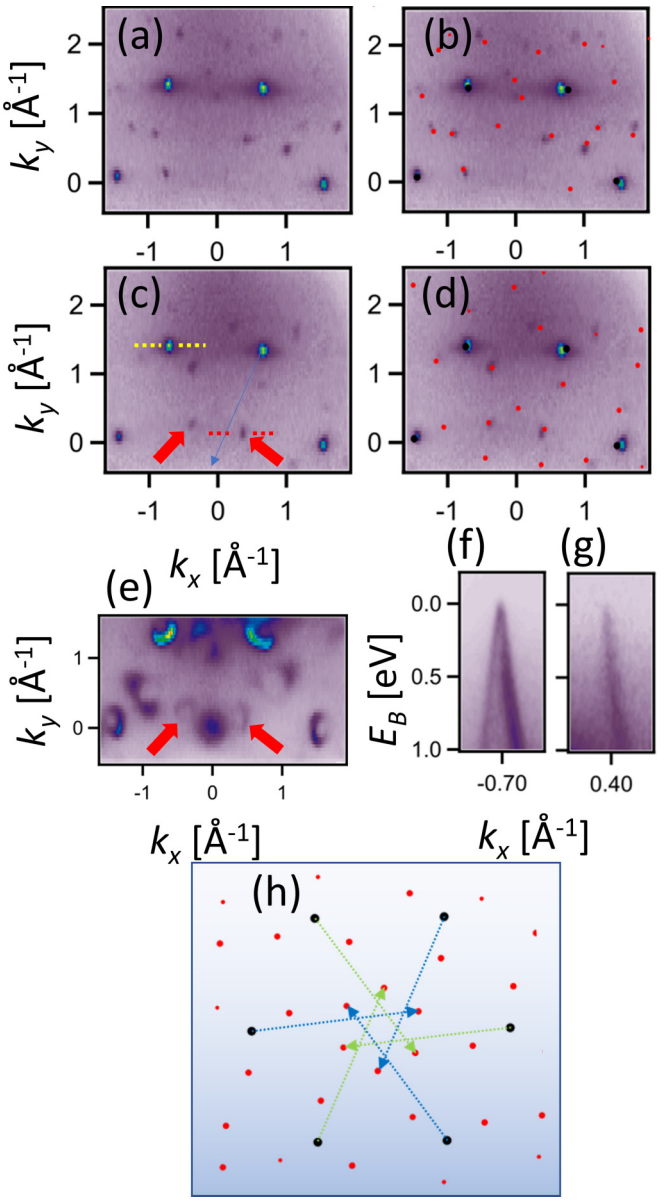

FIG. 8. (a), (b) Fermi level CEMs ($E_B = 30$ meV) for the bottom SL WSe_2/graphite in sample *B*. (c), (d) Same for the top SL WSe_2/graphite in sample *B*. (e) CEM for the top SL WSe_2/graphite at $E_B = 1$ eV. (f), (g) Show $E_B(k_x)$ maps of zero-order graphite *K* point and one of the copies along the trajectories indicated, respectively, by yellow and red dashed lines in (c). Red arrows in (c) and (e) identify selected copies of graphite *K* points, confirming conical shapes of their dispersions. (h) Arrangement of copies related to (d) with indicated $\mathbf{G}_W$ vectors of SL WSe_2. Different colors of the arrows reflect the trigonal symmetry of SL WSe_2.

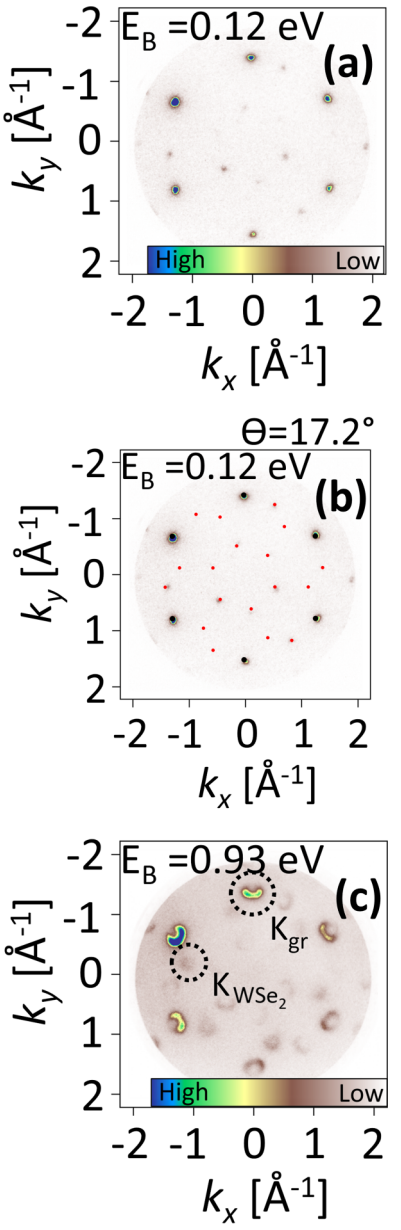

FIG. 9. Maps measured on sample *C* at the NanoESCA beam line with *p*-polarized light at $h\nu = 40$ eV at 80 K. (a) CEM of SL WSe_2/graphite at $E_B = 0.12$ eV. (b) Same as (a) but overlaid with Dirac copies calculated for 17.2° twist angle between WSe_2 and graphite. (c) CEM at $E_B = 0.93$ eV, indicating the *K* points of graphite and WSe_2.

Closer inspection of Figs. 8(b) and 8(d) reveals small discrepancies between the experimental and computed positions of the Dirac copies. We argue that this is related to the nonlinearities of the angular scale in the hemispherical analyzer 2D multi-channel plane (MCP) detector, which might be further influenced by a slight off-axis misalignment of the photon beam spot with respect to the analyzer lens axis. These effects directly translate into momentum scale nonlinearities. ARPES maps can also be measured by an alternative spectrometer design, the so-called *momentum microscope* [47]. In a momentum microscope, the rotational symmetry of the reciprocal space around the sample surface normal is faithfully reproduced through the cylindrical symmetry of the spectrometer lens (due to the momentum microscope design, there is a small binding energy shift of 20–50 meV, in our case along k_y [48], which in principle can be corrected, but has been neglected here). We have performed momentum microscopy at the NanoESCA beam line at Elettra synchrotron on sample *C* which contained SL WSe_2 flake of 20-μm lateral size on graphite (details on sample *C* are in the Supplemental

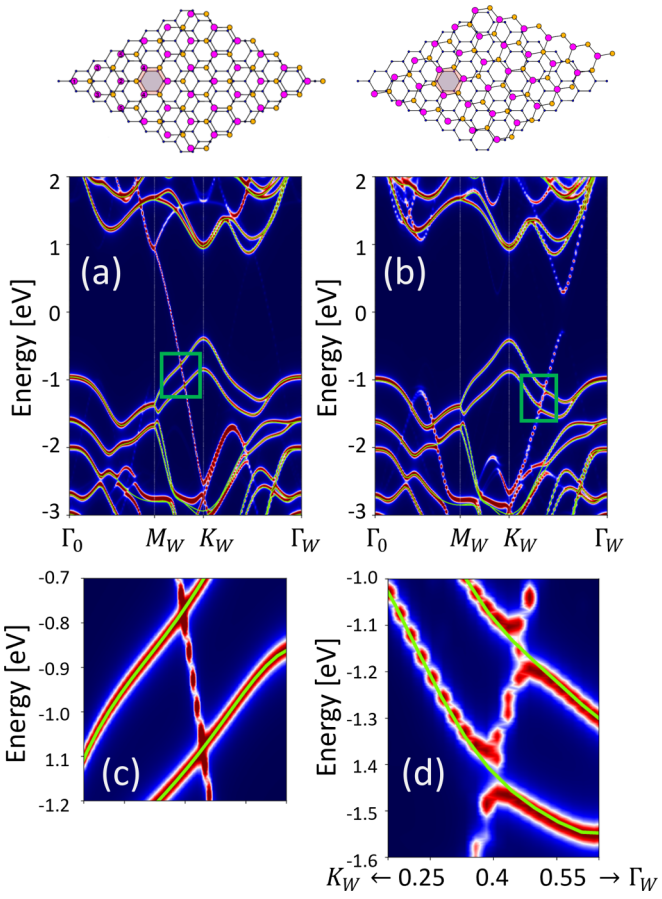

FIG. 10. Theoretical calculations for aligned (a) and 21.79° twisted (b) SL WSe_2 on graphene. The theoretical band structure is deconvoluted onto the Brillouin zone of the freestanding SL WSe_2. (c) and (d) show magnified areas of the green boxes in (a) and (b), respectively. Green lines (in all panels) show the band structure of a freestanding SL WSe_2, for comparison.

Material, Sec. SIII [36]). It was essential to prepare such large flake due to the photon beam spot of 15–20 μm diameter at the NanoESCA beam line. Figure 9 shows the momentum microscope maps from sample *C*. One can see that the overall fitting of the Dirac copies is more accurate as compared to Fig. 8, and allows us to establish the twist angle of ∼17.2° between graphite and SL WSe_2 in sample *C*. Again, the arrangement of copies has a trigonal symmetry, in contrast to zero-order K_{gr} points, which have a hexagonal symmetry.

E. Theoretical calculations of twisted structures

Figure 10 shows theoretical calculations (with SOC included) for the heterobilayer structure (WSe_2/graphene) with 0° and 21.79° hexagonal supercells. The ratio of the experimental WSe_2 to graphene lattice constants is very close to $\frac{4}{3}$, with only ∼0.5% mismatch. Therefore, we modeled the WSe_2/graphene heterostructure containing a 3×3 WSe_2 and a 4×4 graphene supercell [49]. The common lattice constant of this heterostructure is 0.08% larger than freestanding graphene and 0.22% smaller than WSe_2 if the relaxed DFT values are compared. The twisted unit cells are constructed in terms of this common lattice parameter. The 2:1 ratio of the unit vectors gives the twist angle of 21.79°, we define it as $(m, n) = (1, 2)$. A single layer of graphene approximates our experimental graphite substrate.

As shown in Figs. 10(a) and 10(b) for both aligned (0° twist angle) and twisted (21.79° twist angle) SL WSe_2/graphene, there are only minor differences in band positions, as compared to the freestanding SL WSe_2 (green lines), in particular in the region near the VBM. Figure 10(c) shows a magnified region where SL WSe_2 and graphene bands cross for the case of 0° twist angle, where one can see band crossings without significant hybridization gaps. Figure 10(d) shows a similar region, but for the case of 21.79° twist angle. In this case hybridization gaps of the order of 50 meV can be resolved. This finding is probably related to the character of WSe_2 bands at momenta where they cross the graphene band. As shown in Fig. 5(a), the band character changes from in plane at the *K* point into out of plane at Γ. In case of Fig. 10(b) the crossing is further away from the *K* point [as compared to Fig. 10(a)], suggesting less in-plane character, more hybridization, and larger hybridization gaps. This process is competing with the interlayer distance, which is larger for the twisted SL WSe_2/graphene.

Different stacking sequences in the WSe_2 BL have been considered in previous work [17,43]; however, aside from the previously defined AA′ and AA, their nomenclature appears inconsistent. SL WSe_2 has a threefold rotation axis, C_3, without inversion symmetry, therefore, it has polarity in the in-plane direction (along the Γ*M* reciprocal direction). For the bilayer, in the aligned case, there are two general options: either the polarities of the adjacent layers face either in the same direction (such as in the 3*R* bulk polytype) or in opposite directions (the 2H bulk polytype). During the natural growth process, the in-plane shift between the layers is naturally adjusted; however, in the twisted structures it becomes an additional parameter. One can also imagine that at a very small twist angle, the twisted BL will contain large regions of stackings which differ only by that shift, and that the regions of energetically favorable stacking will become larger due to the atomic relaxation.

We focus on the AA and AA′ stackings as starting points for modeling twisted bilayers, with the AA′ stacking being the same as in the most stable 2H polytype, and AA being the two layers directly stacked on top of each other. Starting with AA we considered situations when twisting is either around the center of the W-Se hexagon, around W atoms, or around Se atoms (considering the top view of a BL). Starting with AA′ we only considered twisting around the center of the W-Se hexagon. We define (m, n) and (n, m) as the unit vectors from the top and bottom WSe_2 layers, respectively, that make up the moiré unit cell. This relates to the twist angle θ through $\cos\theta = \frac{1}{2}\frac{m^2+n^2+4mn}{m^2+n^2+mn}$.

We have relaxed the twisted BL WSe_2 structures defined above for several twist angles with the resulting total energy differences and structural information provided in Table I. To reduce the complexity, SOC was not included in these calculations. For the aligned layers, we find the difference ΔE between the most energetically favorable and unfavorable stackings AA′ and AA to be −40.25 meV per W atom in the unit cell. Since the twisted structures contain regions of favorable and unfavorable stackings, their expected energy

TABLE I. The calculated total energies and interlayer distances of twisted BL WSe_2 for the stacking sequence where twisting is around the center of in-plane WSe_2 hexagons. In these calculations SOC was not included. N_W is the number of W atoms per moiré unit cell. ΔE is the energy difference between the AA stacking rotated around the center of the hexagon, as compared to the aligned AA ($\theta = 0$) stacking; $\Delta E = E(\mathrm{AA}) - E_{t,\mathrm{hex}}(\mathrm{AA})$. $\Delta E_{t,\mathrm{hex}} = E_{t,\mathrm{hex}}(\mathrm{AA}') - E_{t,\mathrm{hex}}(\mathrm{AA})$ is the energy difference, between the twisted AA′ and AA stackings with the rotation axis at the center of the hexagon. The energies are given in meV per W atom. The structural parameters (in Å) are given for AA′ stacking twisted around the center of the W-Se hexagon: $\overline{d}_{W-W}$ is the average interlayer out-of-plane distance (along z axis) between W atoms, while Δd is the maximum out-of-plane difference of W atom positions within the layer, it represents the corrugation due to formation of the moiré pattern.

θ	N_W	(m,n)	ΔE	$\Delta E_{t,\mathrm{hex}}$	$\overline{d}_{W-W}$	Δd
21.79°	14	(2,1)	18.50	-0.04	6.839	0.003
13.17°	38	(3,2)	18.73	-0.10	6.842	0.017
7.34°	122	(5,4)	20.20	-0.43	6.814	0.077
6.01°	182	(6,5)	21.04	-0.58	6.813	0.104
3.89°	434	(9,8)	22.56	-0.76	6.768	0.132
0	2	(1,1)	0	-40.25	6.547	0

should be approximately halfway between those of aligned AA′ and AA. This is indeed the case, however, as the twist angle becomes small, the energies, $-\Delta E$, become lower, probably due to extended regions of favorable stacking. The average interlayer distance $\overline{d}_{W-W}$ is larger for larger twist angles, which is again probably related to the larger areas of energetically favorable stacking for smaller twist angles. Accordingly, the corrugation Δd due to the moiré pattern is smaller at larger twist angles.

We also investigated the energy differences $\Delta E_{t,\mathrm{hex}}$ for the layers where the starting stacking is AA or AA′. We find that the difference in energy is smaller for larger twist angles, with the structures starting from AA′ always being more stable. At small twist angles it likely reflects the energy differences between 2H (AA′) and 3R-like stackings which form the areas of favorable stacking.

Figures 11(a)–11(c) show the arrangement of BZs and theoretical band dispersions, with SOC included, for BL WSe_2 at the twist angle 13.17° with twisting around the center of the W-Se hexagon starting with the AA' stacking. Therefore, in absolute terms related to the experimental results of Figs. 2 and 3, the twist angle is $\theta = 60° - 13.17° = 46.83°$. Our actual experimental system consists of BL WSe_2/graphite; however, we omit graphite to reduce numerical complexity. The bands are deconvoluted onto the BZ of one of the layers. As compared to the bands of an aligned AA′ BL WSe_2 shown by green line [see also Fig. 5(b)], the difference near the VBM is mainly in reduced bonding-antibonding splitting of the bands at Γ as indicated by the white rectangle in Fig. 11(b). Figure 11(c) shows the details of the region where anticrossing hybridizations are observed, with the local gaps of the order of 50 meV.

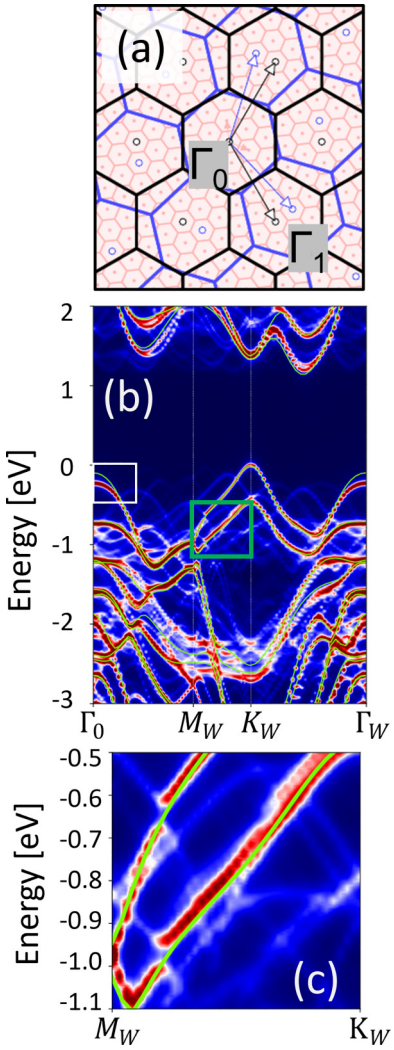

FIG. 11. Theoretical calculations for twisted BL WSe_2 at the twist angle $\theta = 60° - 13.17° = 46.83°$. (a) Black and blue lines depict BZs of the two SLs and the network red lines the moiré BZs of the twisted layers. (b) Band structure unfolded onto the BZ one of the SL WSe_2. (c) Magnified region depicted by the green rectangle in (b). For comparison, green solid lines show the bands for the 2H BL WSe_2.

IV. DISCUSSION

We have performed band mapping on three different SL and two different BL WSe_2 samples placed on graphite. The flakes can be identified in microARPES by rastering the sample with a ∼1 μm photon beam spot, and twist angles between the layers could be established from the CEMs. The hybridization between the WSe_2 and graphene for the twisted structure is predicted to depend on the orbital character of the bands at the crossing points, however, in experimental data no signatures of it could be identified in the uppermost region of valence bands. This might be related to the resolution of our ARPES data or to the increased interlayer distance in our WSe_2/graphite structures, due to a particular twist angle or to impurities trapped between the layers. Accordingly, in the region of the upper valence bands, no dependence of the electronic dispersions on the twist angle between the WSe_2

and graphite has been found, i.e., the spectral features reflect an incoherent sum of the graphite and ML WSe_2 bands. Previously, hybridization effects have been demonstrated for the interface between SL graphene and SL MoS_2 [25,45]; however, the effects were most pronounced at higher binding energies. Our theoretical results indicate that the hybridization may depend sensitively on the twist angle, which might be the reason for these discrepancies.

The electrons emitted from graphite near the Fermi level are focused in K_{gr} points, and we observe diffraction of these electrons when passing through WSe_2. The arrangement of these replicas (sometimes called minibands [19]), which are basically umklapp transitions due to the WSe_2 lattice vectors, can be explained as a final-state effect that would be present also in noninteracting layers. Essentially the same process is expected when shooting the electron beam through a freestanding SL WSe_2. Accordingly, the intensity of the copies follows the trigonal symmetry of a monolayer, bearing similarities to the LEED scattering experiment. Therefore, the existence of such band replicas is an indication of neither a hybridization between the layers nor a moiré-induced potential.

The bonding-antibonding gap at Γ that is a signature of WSe_2 interlayer hybridization persists in our twisted BL WSe_2 microflakes. Its large energy scale of ∼0.4 eV is in stark contrast to negligible hybridization between these bands near Γ from top and bottom layers, as demonstrated in Fig. 4. This is likely related to directional character of the participating Se p_z orbitals that form out-of-plane σ-like bonds but any interlayer in-plane hopping between these out-of-plane orbitals (which can be imagined as π like) is inhibited. Conversely, the in-plane orbital character at K_W points would allow interlayer in-plane σ-like hopping, but this interaction is inhibited by the large interlayer distance of these orbitals that are primarily located on a transition metal.

No indication of flat bands is present in our experimental ARPES maps and our calculations for twisted BL WSe_2 do not indicate any flat bands that are split off from the band structure of separate SLs. For moiré cells larger than in our calculations, recent calculations by Kundu *et al.* [17] identify flat bands over the ∼50 meV energy scale for twist angle up to 5.1°. Small twist angles lead to large moiré unit cells, and to large areas of relatively well-defined stacking areas, which exhibit significantly shifted band structures in the vicinity of Γ, as shown in Figs. 5(b) and 5(c). Our smallest experimental twist angle of ∼10° for BL WSe_2 of sample *A* is too large to allow for formation of experimentally observable gaps between the bands, and in the experimental data small anticrossings might be smeared out. So far, no interlayer hybridization gaps have been reported in microARPES from twisted TMDCs, and the only potential indirect indication of the formation of a moiré potential is through the observation of multiple Dirac copies near the K_{gr} in the graphene/WS_2/WSe_2 heterostructure [20].

In summary, we have described and examined properties of microARPES spectra from several twisted WSe_2 flake samples on graphite substrates. We established that the valence bands maximum of WSe_2 lies at K_W in all studied microstructures. Hybridization effects between twisted BL WSe_2 are manifested in the bonding-antibonding splitting at Γ that are readily observed in the experiment, but do not translate into further emergent interlayer hybridization gaps. Hybridization gaps are also not observed in the studied twisted SL WSe_2/graphite structures. The Fermi level electrons emitted into the K_{gr} points diffract when passing through the WSe_2 overlayer, forming sharp replicas whose positions can be predicted by combining the reciprocal vectors of WSe_2 and graphite. Experimental findings are complemented by theoretical DFT modeling with the inclusion of vdW forces, which suggests that forming of hybridization in WSe_2/graphene system sensitively depends on the orbital character of the WSe_2 at the crossing with the graphene Dirac cone band.

This work paves the way for designing future experiments on twisted TMDC bilayers at smaller twist angles, which would enable imaging their fascinating predicted properties such as topologically nontrivial flat bands.

ACKNOWLEDGMENTS

H.-J.K. acknowledges financial support from the AIDAS project of the Forschungszentrum Jülich and CEA, and from the Alexander von Humboldt Foundation (Grant No. KOR 1211335 HFST-P). B.B., C.S., and L.P. acknowledge support by the Deutsche Forschungsgemeinschaft (DFG, German Research Foundation) under Germany's Excellence Strategy–Cluster of Excellence Matter and Light for Quantum Computing (ML4Q) EXC 2004/1–390534769. L.P. acknowledges financial support from the German Research Foundation (DFG) via the Project No. PL 712/5-1. We gratefully acknowledge the computing time granted through JARA-HPC on the supercomputer JURECA at Forschungszentrum Jülich. This research used resources of the Advanced Light Source, which is a DOE Office of Science User Facility under Contract No. DE-AC02-05CH11231.

[1] H. Yuan, Z. Liu, G. Xu, B. Zhou, S. Wu, D. Dumcenco, K. Yan, Y. Zhang, S. K. Mo, P. Dudin, V. Kandyba, M. Yablonskikh, A. Barinov, Z. Shen, S. Zhang, Y. Huang, X. Xu, Z. Hussain, H. Y. Hwang, Y. Cui *et al.*, Evolution of the valley position in bulk transition-metal chalcogenides and their monolayer limit, Nano Lett. **16**, 4738 (2016).

[2] A. K. Geim and I. V. Grigorieva, Van der Waals heterostructures, Nature **499**, 419 (2013).

[3] N. R. Wilson, P. V. Nguyen, K. Seyler, P. Rivera, A. J. Marsden, Z. P. Laker, G. C. Constantinescu, V. Kandyba, A. Barinov, N. D. Hine, X. Xu, and D. H. Cobden, Determination of band offsets, hybridization, and exciton binding in 2D semiconductor heterostructures, Sci. Adv. **3**, e1601832 (2017).

[4] M. H. Chiu, M. Y. Li, W. Zhang, W. T. Hsu, W. H. Chang, M. Terrones, H. Terrones, and L. J. Li, Spectroscopic signatures for interlayer coupling in MoS_2-WSe_2 van der Waals stacking, ACS Nano **8**, 9649 (2014).

[5] G. Fiori, F. Bonaccorso, G. Iannaccone, T. Palacios, D. Neumaier, A. Seabaugh, S. K. Banerjee, and L. Colombo, Electronics based on two-dimensional materials, Nat. Nanotechnol. **9**, 768 (2014).

[6] L. Wang, E. M. Shih, A. Ghiotto, L. Xian, D. A. Rhodes, C. Tan, M. Claassen, D. M. Kennes, Y. Bai, B. Kim, K. Watanabe, T. Taniguchi, X. Zhu, J. Hone, A. Rubio, A. N. Pasupathy, and C. R. Dean, Correlated electronic phases in twisted bilayer transition metal dichalcogenides, Nat. Mater. **19**, 861 (2020).

[7] S. Manzeli, D. Ovchinnikov, D. Pasquier, O. V. Yazyev, and A. Kis, 2D transition metal dichalcogenides, Nat. Rev. Mater. **2**, 17033 (2017).

[8] F. H. Koppens, T. Mueller, P. Avouris, A. C. Ferrari, M. S. Vitiello, and M. Polini, Photodetectors based on graphene, other two-dimensional materials and hybrid systems, Nat. Nanotechnol. **9**, 780 (2014).

[9] G. R. Bhimanapati, Z. Lin, V. Meunier, Y. Jung, J. Cha, S. Das, D. Xiao, Y. Son, M. S. Strano, V. R. Cooper, L. Liang, S. G. Louie, E. Ringe, W. Zhou, S. S. Kim, R. R. Naik, B. G. Sumpter, H. Terrones, F. Xia, Y. Wang *et al.*, Recent Advances in Two-Dimensional Materials beyond Graphene, ACS Nano **9**, 11509 (2015).

[10] F. Volmer, M. Ersfeld, P. E. F. Junior, L. Waldecker, B. Parashar, L. Rathmann, S. Dubey, I. Cojocariu, V. Feyer, K. Watanabe *et al.*, Twist angle dependent interlayer transfer of valley polarization from excitons to free charge carriers in $WSe_2/MoSe_2$ heterobilayers, arXiv:2211.17210.

[11] F. He, Y. Zhou, Z. Ye, S.-H. Cho, J. Jeong, X. Meng, and Y. Wang, Moiré patterns in 2D materials: A review, ACS Nano **15**, 5944 (2021).

[12] R. Bistritzer and A. H. MacDonald, Moiré bands in twisted double-layer graphene, Proc. Natl. Acad. Sci. USA **108**, 12233 (2011).

[13] Y. Cao, V. Fatemi, S. Fang, K. Watanabe, T. Taniguchi, E. Kaxiras, and P. Jarillo-Herrero, Unconventional superconductivity in magic-angle graphene superlattices, Nature **556**, 43 (2018).

[14] F. Wu, T. Lovorn, E. Tutuc, and A. H. MacDonald, Hubbard Model Physics in Transition Metal Dichalcogenide Moiré Bands, Phys. Rev. Lett. **121**, 026402 (2018).

[15] M. H. Naik and M. Jain, Ultraflatbands and Shear Solitons in Moiré Patterns of Twisted Bilayer Transition Metal Dichalcogenides, Phys. Rev. Lett. **121**, 266401 (2018).

[16] F. Wu, T. Lovorn, E. Tutuc, I. Martin, and A. H. MacDonald, Topological Insulators in Twisted Transition Metal Dichalcogenide Homobilayers, Phys. Rev. Lett. **122**, 086402 (2019).

[17] S. Kundu, M. H. Naik, H. R. Krishnamurthy, and M. Jain, Moiré induced topology and flat bands in twisted bilayer WSe_2: A first-principles study, Phys. Rev. B **105**, L081108 (2022).

[18] M. Cattelan and N. Fox, A Perspective on the Application of Spatially Resolved ARPES for 2D Materials, Nanomaterials **8**, 284 (2018).

[19] S. Ulstrup, R. J. Koch, S. Singh, K. M. McCreary, B. T. Jonker, J. T. Robinson, C. Jozwiak, E. Rotenberg, A. Bostwick, J. Katoch, and J. A. Miwa, Direct observation of minibands in a twisted graphene/WS_2 bilayer, Sci. Adv. **6**, eaay6104 (2020).

[20] S. Xie, B. D. Faeth, Y. Tang, L. Li, C. T. Parzyck, D. Chowdhury, Y.-H. Zhang, C. Jozwiak, A. Bostwick, E. Rotenberg, E.-A. Kim, J. Shan, K. F. Mak, and K. M. Shen, Strong interlayer interactions in bilayer and trilayer moiré superlattices, Sci. Adv. **8**, eabk1911 (2022).

[21] A. J. H. Jones, R. Muzzio, S. Pakdel, D. Biswas, D. Curcio, N. Lanatà, P. Hofmann, K. M. McCreary, B. T. Jonker, K. Watanabe, T. Taniguchi, S. Singh, R. J. Koch, C. Jozwiak, E. Rotenberg, A. Bostwick, J. A. Miwa, J. Katoch, and S. Ulstrup, Visualizing band structure hybridization and superlattice effects in twisted MoS_2/WS_2 heterobilayers, 2D Mater. **9**, 015032 (2022).

[22] S. Lisi, X. Lu, T. Benschop, T. A. de Jong, P. Stepanov, J. R. Duran, F. Margot, I. Cucchi, E. Cappelli, A. Hunter, A. Tamai, V. Kandyba, A. Giampietri, A. Barinov, J. Jobst, V. Stalman, M. Leeuwenhoek, K. Watanabe, T. Taniguchi, L. Rademaker *et al.*, Observation of flat bands in twisted bilayer graphene, Nat. Phys. **17**, 189 (2021).

[23] M. I. B. Utama, R. J. Koch, K. Lee, N. Leconte, H. Li, S. Zhao, L. Jiang, J. Zhu, K. Watanabe, T. Taniguchi, P. D. Ashby, A. Weber-Bargioni, A. Zettl, C. Jozwiak, J. Jung, E. Rotenberg, A. Bostwick, and F. Wang, Visualization of the flat electronic band in twisted bilayer graphene near the magic angle twist, Nat. Phys. **17**, 184 (2021).

[24] S. Agnoli, A. Ambrosetti, T. O. Menteş, A. Sala, A. Locatelli, P. L. Silvestrelli, M. Cattelan, S. Eichfeld, D. D. Deng, J. A. Robinson, J. Avila, C. Chen, and M. C. Asensio, Unraveling the Structural and Electronic Properties at the WSe_2-Graphene Interface for a Rational Design of van der Waals Heterostructures, ACS Appl. Nano Mater. **1**, 1131 (2018).

[25] D. Pierucci, H. Henck, J. Avila, A. Balan, C. H. Naylor, G. Patriarche, Y. J. Dappe, M. G. Silly, F. Sirotti, A. T. Johnson, M. C. Asensio, and A. Ouerghi, Band alignment and minigaps in monolayer MoS_2-graphene van der Waals heterostructures, Nano Lett. **16**, 4054 (2016).

[26] A. Castellanos-Gomez, M. Buscema, R. Molenaar, V. Singh, L. Janssen, H. S. Van Der Zant, and G. A. Steele, Deterministic transfer of two-dimensional materials by all-dry viscoelastic stamping, 2D Mater. **1**, 011002 (2014).

[27] R. J. Koch, C. Jozwiak, A. Bostwick, B. Stripe, M. Cordier, Z. Hussain, W. Yun, and E. Rotenberg, Nano focusing of soft x-rays by a new capillary mirror optic, Synchrotron Radiat. News **31**, 50 (2018).

[28] G. Kresse and J. Furthmüller, Efficient iterative schemes for ab initio total-energy calculations using a plane-wave basis set, Phys. Rev. B **54**, 11169 (1996).

[29] G. Kresse and J. Hafner, Ab initio molecular dynamics for liquid metals, Phys. Rev. B **47**, 558 (1993).

[30] P. E. Blöchl, Projector augmented-wave method, Phys. Rev. B **50**, 17953 (1994).

[31] I. Hamada, Van der Waals density functional made accurate, Phys. Rev. B **89**, 121103(R) (2014).

[32] H. Peng, Z. H. Yang, J. P. Perdew, and J. Sun, Versatile van der Waals Density Functional Based on a Meta-Generalized Gradient Approximation, Phys. Rev. X **6**, 041005 (2016).

[33] H. J. Kim, S. H. Kang, I. Hamada, and Y. W. Son, Origins of the structural phase transitions in $MoTe_2$ and WTe_2, Phys. Rev. B **95**, 180101(R) (2017).

[34] V. Popescu and A. Zunger, Extracting E versus $\vec{k}$ effective band structure from supercell calculations on alloys and impurities, Phys. Rev. B **85**, 085201 (2012).

[35] H.-J. Kim, VASPBAUM (2021), https://github.com/Infant83/VASPBAUM.

[36] See Supplemental Material at http://link.aps.org/supplemental/10.1103/PhysRevMaterials.7.044004 for additional details of experimental methods.

[37] Y. Zhang, M. M. Ugeda, C. Jin, S. F. Shi, A. J. Bradley, A. Martín-Recio, H. Ryu, J. Kim, S. Tang, Y. Kim, B. Zhou, C. Hwang, Y. Chen, F. Wang, M. F. Crommie, Z. Hussain, Z. X. Shen, and S. K. Mo, Electronic structure, surface doping, and optical response in epitaxial WSe_2 thin films, Nano Lett. **16**, 2485 (2016).

[38] P. V. Nguyen, N. C. Teutsch, N. P. Wilson, J. Kahn, X. Xia, A. J. Graham, V. Kandyba, A. Giampietri, A. Barinov, G. C. Constantinescu, N. Yeung, N. D. M. Hine, X. Xu, D. H. Cobden, and N. R. Wilson, Visualizing electrostatic gating effects in two-dimensional heterostructures, Nature **572**, 220 (2019).

[39] S. Moser, An experimentalist's guide to the matrix element in angle resolved photoemission, J. Electron Spectrosc. Relat. Phenom. **214**, 29 (2017).

[40] J. Braun, J. Minár, and H. Ebert, Correlation, temperature and disorder: Recent developments in the one-step description of angle-resolved photoemission, Phys. Rep. **740**, 1 (2018).

[41] M. Gehlmann, I. Aguilera, G. Bihlmayer, E. Młyńczak, M. Eschbach, S. Döring, P. Gospodarič, S. Cramm, B. Kardynał, L. Plucinski, S. Blügel, and C. M. Schneider, Quasi 2D electronic states with high spin-polarization in centrosymmetric MoS_2 bulk crystals, Sci. Rep. **6**, 26197 (2016).

[42] T. Heider, G. Bihlmayer, J. Schusser, F. Reinert, J. Minár, S. Blügel, C. M. Schneider, and L. Plucinski, Geometry-induced spin-filtering in photoemission maps from WTe_2 surface states, arXiv:2210.10870.

[43] J. He, K. Hummer, and C. Franchini, Stacking effects on the electronic and optical properties of bilayer transition metal dichalcogenides MoS_2, $MoSe_2$, WS_2, and WSe_2, Phys. Rev. B **89**, 075409 (2014).

[44] H. Nakamura, A. Mohammed, P. Rosenzweig, K. Matsuda, K. Nowakowski, K. Küster, P. Wochner, S. Ibrahimkutty, U. Wedig, H. Hussain, J. Rawle, C. Nicklin, B. Stuhlhofer, G. Cristiani, G. Logvenov, H. Takagi, and U. Starke, Spin splitting and strain in epitaxial monolayer WSe_2 on graphene, Phys. Rev. B **101**, 165103 (2020).

[45] H. Coy Diaz, J. Avila, C. Chen, R. Addou, M. C. Asensio, and M. Batzill, Direct observation of interlayer hybridization and Dirac relativistic carriers in Graphene/MoS_2 van der Waals heterostructures, Nano Lett. **15**, 1135 (2015).

[46] I. Gierz, J. Henk, H. Höchst, C. R. Ast, and K. Kern, Illuminating the dark corridor in graphene: Polarization dependence of angle-resolved photoemission spectroscopy on graphene, Phys. Rev. B **83**, 121408(R) (2011).

[47] C. Tusche, A. Krasyuk, and J. Kirschner, Spin resolved bandstructure imaging with a high resolution momentum microscope, Ultramicroscopy **159**, 520 (2015).

[48] C. Tusche, Y.-J. Chen, C. M. Schneider, and J. Kirschner, Imaging properties of hemispherical electrostatic energy analyzers for high resolution momentum microscopy, Ultramicroscopy **206**, 112815 (2019).

[49] M. Gmitra, D. Kochan, P. Högl, and J. Fabian, Trivial and inverted Dirac bands and the emergence of quantum spin Hall states in graphene on transition-metal dichalcogenides, Phys. Rev. B **93**, 155104 (2016).